Catalysis Science & Technology

Accepted Manuscript

ROYAL SOCIETY OF CHEMISTRY

www.rsc.org/catalysis

Cite this: DOI: 10.1039/c0xx00000x

www.rsc.org/xxxxxx

ARTICLE TYPE

Highly efficient nanosized Mn and Fe codoped ceria-based solid solutions for elemental mercury removal at low flue gas temperatures

Deshetti Jampaiah[a,b], Samuel J. Ippolito[b], Ylias M. Sabri[b], Benjaram M. Reddy*[a] and Suresh K. Bhargava*[b]

Received (in XXX, XXX) Xth XXXXXXXXX 20XX, Accepted Xth XXXXXXXXX 20XX
DOI: 10.1039/b000000x

Abstract Ceria (CeO_2) is a well-known material for various industrial applications due to its unique redox properties. Such properties, dominated by structural defects that are primarily oxygen vacancies associated with the Ce^{3+}/Ce^{4+} redox couple, can be easily modulated and optimized by different approaches. In this paper, nanosized Mn and Fe codoped CeO_2 solid solutions, $Ce_{0.7-x}Mn_{0.3}Fe_xO_{2-\delta}$ (x= 0.05–0.2) were prepared by a simple coprecipitation method and tested towards elemental mercury (Hg^0) oxidation and adsorption. The obtained solid solutions were characterized in detail at the structural and electronic level by various techniques, namely, XRD, ICP-OES, BET surface area, TEM, Raman, H_2–TPR, and XPS. The XRD results suggest that the Mn and/or Fe dopant cations are effectively incorporated into the CeO_2 lattice. BET surface area results suggest that the addition of Mn and/or Fe dopants to CeO_2 significantly reduces its crystallite size, and thereby improve the surface area. Raman, H_2–TPR, and XPS results reveal that the Mn and/or Fe dopant cations in the ceria lattice increased the concentration of structural oxygen vacancies and the reducibility of the redox pair Ce^{4+}/Ce^{3+}. The Hg^0 oxidation and adsorption studies indicate that $Ce_{0.7-x}Mn_{0.3}Fe_xO_{2-\delta}$ solid solutions exhibited highest activity compared to pure CeO_2. In particular, the $Ce_{0.5}Mn_{0.3}Fe_{0.2}O_{2-\delta}$ (CMF20) solid solution shows Hg^0 oxidation efficiency (E_{oxi}) of 86.5 %. It can be demonstrated that Mn and Fe doping together led to lattice distortion and restrained grain growth of CeO_2, yielding a synergistic effect in increasing more oxygen vacancies and catalytic activity.

1. Introduction

Mercury is one of the major lethal pollutants due to its toxicity, mobility and bioaccumulation in the ecosystem and food chain.[1] Once it enters water bodies through air deposition, inorganic mercury can be methylated biotically to its most toxic form, dimethyl mercury ($(CH_3)_2Hg$), under anaerobic conditions. Thereafter it is able to enter the human body through food chain, where it can be lead to nervous system disorders, kidney and liver damage, and impaired childhood development.[2,3] Due to its adverse health effects to human and the environment, the abatement of mercury has attracted an enormous public interest in recent years. Among various emission sources, coal-fired power plants are the largest single-known source of anthropogenic mercury emissions. Therefore, the mitigation of mercury emission from coal-fired power plants is a worldwide objective. The emitted mercury exists in three different forms, namely, particulate-bound (Hg_p), oxidized (Hg^{2+}), and elemental (Hg^0).[4]

[a]RMIT-IICT Joint Research Centre, CSIR-Indian Institute of Chemical Technology, Uppal Road, Hyderabad – 500 607, India E–mail addresses: bmreddy@iict.res.in; mreddyb@yahoo.com Phone: +91 40 2719 3510; fax: +91 40 2716 0921.
[b]Centre for Advanced Materials & Industrial Chemistry (CAMIC), School of Applied Sciences, RMIT University, GPO BOX 2476, Melbourne–3001, Australia. E-mail: suresh.bhargava@rmit.edu.in; Tel: +61 3 9925 3365

It is well known that Hg_p can be removed by various conventional air pollution control technologies such as electrostatic precipitators (ESP), fabric filters, and baghouses. The oxidized form of mercury (Hg^{2+}) can be captured efficiently by wet scrubber. However, the conventional technologies have little effect on Hg^0 removal. Therefore, the removal of Hg^0 is quite demanding and has received significant attention.

Among the available technologies, sorbent technology and catalytic oxidation of Hg^0 to Hg^{2+} have attracted renewed interest to reduce Hg^0 emissions from coal-fired power plants. Primarily, the activated carbon sorbents were widely exploited for Hg^0 emission control due to their higher surface area and more surface reactivity. Additionally, activated carbon functionalised with metal oxides, such as CuO, MnO_2, Fe_2O_3, TiO_2 and V_2O_5 have been studied broadly to improve the Hg^0 removal efficiency.[4] Such metal oxides have also been used as alternative to carbon based sorbents due to their improved regeneration ability over carbon, thus improving the overall removal performance and reduce operating costs for the mercury control systems. Moreover, Granite et al. found that sorbents supported with noble metals such as iridium, platinum, palladium and ruthenium effectively remove Hg^0 from simulated flue gas at temperatures of 477–644 K.[5] However, the application and development of activated carbon injection technology is limited due to their exorbitant price and lower utilization rate, especially at higher temperatures.[6] Furthermore, Hg^0 capture by injection of activated carbon is not ideal because the discharged activated carbon with

fly ash can increase the carbon content, thereby decreases the ash's value.[7] Due to these concerns, the catalytic oxidation process ($Hg^0 \rightarrow Hg^{2+}$) by using metal oxides has attracted significant attention for effective Hg^0 control systems.

Up to present, various metal oxide catalysts for Hg^0 removal studied mainly fall into two groups, namely, selective catalytic reduction (SCR) catalysts, and transition metal oxide catalysts.[8,9] Among various SCR catalysts, a widely employed material is titania supported vanadium and tungsten oxides (V_2O_5–WO_3/TiO_2) and it was reported that the active vanadia phase, V_2O_5, can be responsible for better Hg^0 oxidation and/or NO_x reduction as well as other catalytic applications.[10,11] Here, the promising advantage of conventional vanadia based SCR catalysts is the co-benefit of promoting Hg^0 oxidation along with NO_x reduction in coal-fired power plants. However, there is a possibility of deactivation when the catalyst is exposed to high concentrations of particulate matter (PM) in SCR installed power plants at higher temperatures (573–673 K).[12] Additionally, there are some drawbacks such as loss of V_2O_5 during synthesis as well as harmful nature of V_2O_5 based catalysts to the environment and human health.[13] In order to overcome these concerns, it is significant to develop a material with high activity at low temperatures (373–523 K). Recently, it is well acknowledged in the literature that transition metal oxide-based catalysts have potential preponderance to remove both Hg^0 and Hg^{2+} by means of adsorption and oxidation.[14] The Hg^0 removal process occurs at relatively low temperatures as well as the thermal decomposition of Hg^{2+} to Hg^0 can be inhibited. Among various metal oxides, the combination of MnO_x and TiO_2 with CeO_2 has been conducted to develop effective Hg^0 oxidation technologies because of their various applications such as selective catalytic reduction (SCR), carbon monoxide (CO) oxidation, as well as water-gas shift reactions. [15–18] It is strongly believed that the properties such as large oxygen storage capacity (OSC) and superior redox behavior of Ce^{3+}/Ce^{4+} could be useful in enhancing Hg^0 oxidation efficiency. Li et al. observed a significant synergy for Hg^0 oxidation when MnO_x and CeO_2 were combined and they reported that TiO_2 supported MnO_x–CeO_2 catalyst was highly active for Hg^0 oxidation under simulated flue gas at 473−523 K.[18] The performance of these materials is mainly due to their extent of OSC and oxygen vacancy concentration.[13,19] Therefore, it is highly desirable to increase the active oxygen content of CeO_2–MnO_x based materials for Hg^0 oxidation at low operating temperatures. In order to further increase the oxygen vacancy concentration and improve other related properties of the CeO_2–MnO_x materials, codoping approach has been reported to be a feasible option. So far various studies have been conducted to improve OSC and oxygen mobility by modifying ceria structure through the doping of various cations such as Zr, Zn, Co, Ni, Cu, and Fe.[20–22] Such modification of ceria is related to structural distortions of the fluorite phase produced by the dopant cations. Among the various dopant cations, Fe has the special advantages of strong toxicity resistance and high catalytic activity owing to various applications, such as the catalytic oxidation of CO.[23] To the authors' knowledge, the related research on Mn and Fe codoped ceria catalysts for Hg^0 oxidation and adsorption has rarely been reported in the literature. Therefore, a better knowledge about performance and mechanism of Hg^0 adsorption and oxidation over Mn and Fe codoped ceria catalysts is required.

In this work, the $Ce_{0.7-x}Mn_{0.3}Fe_xO_{2-\delta}$ (x= 0.05, 0.1, 0.15, and 0.2) solid solutions prepared by a simple coprecipitation method were employed to oxidize Hg^0 to Hg^{2+} under simulated flue gas conditions. An effect of catalyst composition was investigated as well. First, Mn and Fe codoped CeO_2 solid solutions were synthesized by coprecipitation method through codoping approach and the as-prepared catalysts were characterized by using various techniques, namely, X-ray diffraction (XRD), inductively coupled plasma-optical emission spectroscopy (ICP-OES), Brunauer–Emmett–Teller (BET) surface area, pore size distribution, transmission electron microscopy (TEM), Raman spectroscopy (RS), hydrogen-temperature programmed reduction (H_2-TPR), and X-ray photoelectron spectroscopy (XPS). Second, the mechanism involved in Hg^0 oxidation and adsorption was examined in presence of different flue gas components such as HCl, O_2, HCl/O_2, and NH_3.

2. Experimental

2.1. Catalyst preparation

The $Ce_{0.7-x}Mn_{0.3}Fe_xO_{2-\delta}$ (where the molar ratio, x= 0.05, 0.1, 0.15, and 0.2) solid solutions were prepared by a coprecipitation method using $Ce(NO_3)_3.6H_2O$ (*Aldrich, AR grade*), $Mn(NO_3)_2.4H_2O$ (*Merck, AR grade*), and $Fe(NO_3)_2.9H_2O$ (*Merck, AR grade*) precursors. In a typical procedure, requisite quantities of precursors were dissolved separately in deionized water and mixed together. After, the aqueous NH_3 was added drop-wise with vigorous stirring until the precipitation was complete (pH ~9). The resulting product was filtered off, washed several times with deionized water until it was free from ion impurities (i.e NH_4^+ and NO_3^-), and then oven dried at 383 K for 12 h. Finally, the catalysts were calcined at 773 K for 5 h in air atmosphere. For comparison, $Ce_{0.7}Mn_{0.3}O_{2-\delta}$ and pure CeO_2 were also prepared by the same method. The as-prepared $Ce_{0.7}Mn_{0.3}O_{2-\delta}$, $Ce_{0.65}Mn_{0.3}Fe_{0.05}O_{2-\delta}$, $Ce_{0.6}Mn_{0.3}Fe_{0.1}O_{2-\delta}$, $Ce_{0.55}Mn_{0.3}Fe_{0.15}O_{2-\delta}$, and $Ce_{0.5}Mn_{0.3}Fe_{0.2}O_{2-\delta}$ catalysts are designated as CM, CMF5, CMF10, CMF15, and CMF20, respectively.

2.2. Catalyst characterization

The X-ray diffraction patterns of the samples were recorded using a Rigaku Multiflex diffractometer that was equipped with a nickel-filtered Cu-Kα (1.5418 Å) radiation source as well as a scintillation counter detector. The diffractograms were recorded over a 2θ range of 10 to 80° with a step size of 0.021 and the step time of 1 s per point. The Scherrer equation was used to calculate the mean crystallite size (D) and the cell parameters (*a*) of various catalysts were determined by a standard cubic indexation method using the intensity of the (111) peak.

Inductively coupled plasma-optical emission spectroscopy (ICP-OES, Thermo Jarrel Ash model IRIS Intrepid II XDL, USA) was used to confirm the respective concentrations of elements in the system. For ICP analysis, approximately 50 mg of the sample was dissolved in a solution of 25 ml aqua regia and

475 ml distilled water. Then 10 ml of the above solution was diluted to 250 ml before analysis.

The surface areas and pore size distribution of the as-prepared catalysts were measured using N_2 adsorption-desorption isotherms obtained from a Micromeritics (ASAP 2000) analyzer which was set at a liquid N_2 temperature of 77 K. Specific surface area and pore size distribution were calculated by Brunauer-Emmett-Teller (BET) and Barrett-Joyner-Halenda (BJH) methods, respectively.

Transmission electron microscopy (TEM) images were obtained by using a JEOL-1010 microscope. Samples for TEM analysis were dispersed in ethyl alcohol by ultrasonication. A drop of the dilute suspension was then placed on a perforated-carbon-coated copper grid for TEM analysis.

Raman spectra were collected on a DILORXY spectrometer using an Ar^+ ion laser beam with an excitation wavelength of 632 nm. The instrument was equipped with a liquid N_2 cooled detector. The spectra obtained from the instrument had a precision within 2 cm^{-1}.

H_2-temperature programmed reduction (H_2-TPR) experiments were performed using a gas chromatograph (Shimadzu) with a thermal conductivity based detector. The sample (30 mg) was loaded in an isothermal zone of the reactor and pre-treated in a helium gas flow at 473 K and then cooled to room temperature before conducting the H_2-TPR analysis. Then, the TPR started from an ambient temperature to the target temperature in a 20 mL min^{-1} flow made up of 5% H_2 balanced in Ar gas at a rate of 10 K min^{-1}.

X-ray photoelectron spectroscopy (XPS) analysis was performed on a Thermo Scientific K-Alpha instrument (un-monochromatized Mg Kα radiation, photon energy of 1253.6 eV at vacuum better than 10^{-9} Torr). The sample charging effects were corrected by referencing the spectra to the carbon (C 1s) peak at 285 eV.

2.3. Catalyst activity studies

Fig. S1 shows the bench-scale experimental system used for Hg^0 removal studies. The apparatus consists of temperature-controlled quartz reactor, mercury speciation trapping system, HCl vapor generator and Hg^0 vapor generator. The total gas flow rate was set at 0.2 L min^{-1} when conducting Hg^0 removal tests. A mercury permeation device (VICI, Metronics Inc.) was used as the Hg^0 source that generated Hg^0 vapor concentration of ~320 µg m^{-3}, which is much lower than the saturation level of Hg^0 in air at room temperature (14.1 mg m^{-3}). Similarly, hydrogen chloride vapor was generated using HCl permeation device (VICI, Metronics Inc.) which was placed inside an in-house built Teflon cell that was temperature controlled to 62 ± 0.1°C thus producing HCl concentration of 64 mg m^{-3}. Dry N_2 gas was used as the carrier gas in order to deliver the permeated HCl and Hg^0 vapor out of the generators. The flow rate of each individual flue gas was controlled to within ±1% by using mass flow controllers (John Morris Scientific). The typical composition of a simulated flue gas mixture was 10 ppm HCl, 3% O_2, 5% CO_2, and 300 ppm NH_3, and balanced with dry N_2. In order to support the catalyst layer and avoid any loss, the reactor was loaded with a small portion of quartz wool before loading with the catalyst material. For each experiment, ~0.4 g of the prepared catalysts was loaded into the centre of the reactor bed and the reactor was gradually heated to reach the desired temperature (423 K). The catalyst mass was chosen based on the geometry of the catalyst bed reactor diameter (Ø = 1 cm) in the experimental setup as well as enable to perform catalyst digestion in mass balance experiments. As part of the experiment, the catalyst was exposed to simulated flue gas for a period of 16 h. In order to ensure the steady-state operation of the system, the Hg^0 stream was first directed towards the exhaust for a period of 1 hour before being directed towards the catalyst bed reactor. Thereafter, the outlet gas stream was passed through a series of seven impingers to capture and speciate the outlet mercury. In this work, the arrangement of the traps was based on a variant of the Ontario Hydro Method (OHM), in which the flue gas is passed through an absorbing media (KCl and $KMnO_4$ solutions).[24] Then, the samples of the absorbing media are quantitatively analyzed for their Hg contents using an inductively coupled plasma mass spectrometer (Agilent 7700 Series, ICP-MS). The KCl impinger solutions were used to capture the Hg^{2+}, whereas $KMnO_4$ containing impinger solutions were used to capture the non-oxidised portion. According to OHM, the oxidised mercury is calculated as the sum of mercury measured in the KCl impinger solutions, while the elemental mercury is the sum of the mercury measured in the $KMnO_4$ impinger solutions. The adsorbed mercury was then determined by digesting the spent catalyst following the 16 hour testing period. In this procedure, a known amount of sample was combined with 1 mL of aqua regia and one drop of $KMnO_4$ and then aged for overnight at room temperature. The purpose of the $KMnO_4$ in the digest media was to absorb any mercury evolved in the closed container due to the heat released during the digestion process, allowing the total amount of mercury to be determined using ICP-MS analysis. This digestion step together with the OHM method allows a full mass balance. To establish a baseline prior to conducting the catalysis experiment, the total inlet mercury (Hg^0_{inlet}) was determined by performing a calibration experiment without the presence of any catalyst in the system. The adsorbed mercury can also be considered as oxidised mercury (i.e. HgO). Based on this data, the Hg^0 removal performances are categorized into two definitions such as oxidation efficiency (E_{oxi}, %) and adsorption efficiency (E_{ads}, %). The Hg^0 oxidation efficiency (E_{oxi}) and the Hg^0 adsorption efficiency (E_{ads}) of the developed catalysts were determined by using the following equations:

$$E_{oxi}(\%) = \frac{Hg^{2+}}{Hg^0_{in}} \times 100 \quad (1)$$

$$E_{ads}(\%) = \frac{Hg_{ads}}{Hg^0_{in}} \times 100 \quad (2)$$

3. Results and discussion

3.1. Characterization studies

The XRD patterns of CM and CMF samples are shown in Fig. 1. For comparison, pure CeO_2 XRD pattern is also included. The distinct diffraction peaks in the XRD pattern of CM sample can be indexed to the CeO_2 (111), (200), (220), (311), and (222) lattice planes, which can be attributed to the fluorite structure of CeO_2 as identified by using the standard data JCPDS 34-0394.[25] There are no secondary phases such as Mn_3O_4, Mn_2O_3, MnO in the XRD profiles of CM sample indicating the formation of $Ce_{0.7}Mn_{0.3}O_{2-\delta}$ solid solution. However, it cannot be ruled out that some portion of amorphous Mn-oxide phases might exist on the surface of the nanocomposite mixed oxide.[26] The XRD patterns of CMF5, CMF10, CMF15, and CMF20 samples also show the same diffraction peaks as that of pure CeO_2. Further, the diffraction peaks derived from Fe_3O_4, Fe_2O_3, or FeO phases are absent in these samples. It can be concluded that Mn and/or Fe dopant cations clearly substitute into CeO_2 lattice, which may be due to the increased solubility of Mn as a result of codoping with Fe.[27] XRD analysis also reveals that all peaks for CMF samples were significantly wider compared to pure CeO_2 sample and it clearly confirmed that broadening indicates small crystallite size and/or strain.

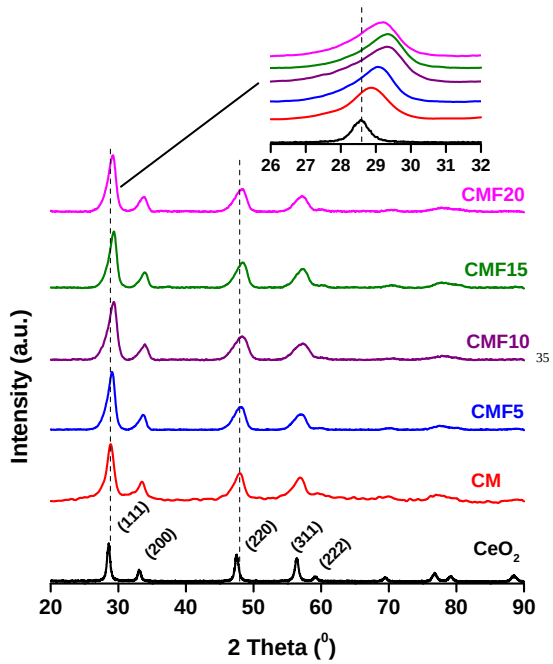

Fig. 1 XRD patterns of CeO_2, $Ce_{0.7}Mn_{0.3}O_{2-\delta}$ (CM), $Ce_{0.65}Mn_{0.3}Fe_{0.05}O_{2-\delta}$ (CMF5), $Ce_{0.6}Mn_{0.3}Fe_{0.1}O_{2-\delta}$ (CMF10), $Ce_{0.55}Mn_{0.3}Fe_{0.15}O_{2-\delta}$ (CMF15), and $Ce_{0.5}Mn_{0.3}Fe_{0.2}O_{2-\delta}$ (CMF20) catalysts.

The average crystallite sizes of all samples were calculated from X-ray line broadening of the peaks at (111) lattice plane by using Sherrer's equation and illustrated in Table 1. It can be confirmed that the pure ceria and CM samples show crystallite sizes of 8.92 and 7.19 nm, respectively. Interestingly, the CMF samples show a remarkable decrease in crystallite size and the observed values are in the range of 5.89–7.02 nm. It clearly indicates that the substitution of Mn and/or Fe together into the CeO_2 lattice diminished the crystallite growth largely due to the appearance of oxygen vacancies and lattice defects in the CeO_2 lattice.[28, 29] The inset of Fig. 1 shows that the 2θ value of (111) plane of CM sample shift slightly towards higher angles compared to pure CeO_2. In the case of CMF samples, the shift was more pronounced. To understand this, the lattice parameters (*a*) were estimated and illustrated in Table 1. The lattice parameter calculated from the (111) reflection of the pure CeO_2 nanoparticles is 5.413 Å (Table 1), which matches well with the lattice parameter of bulk CeO_2 (a=5.411Å).[30, 31] The large cell parameter may be attributed to the lattice defects resulting from the increased Ce^{3+} ions and oxygen vacancies. Similarly, the lattice parameter values were calculated for CM and CMF samples and the values are in the range of 5.29–5.35 Å, which is smaller than pure CeO_2. It can be confirmed that a clear decrease-

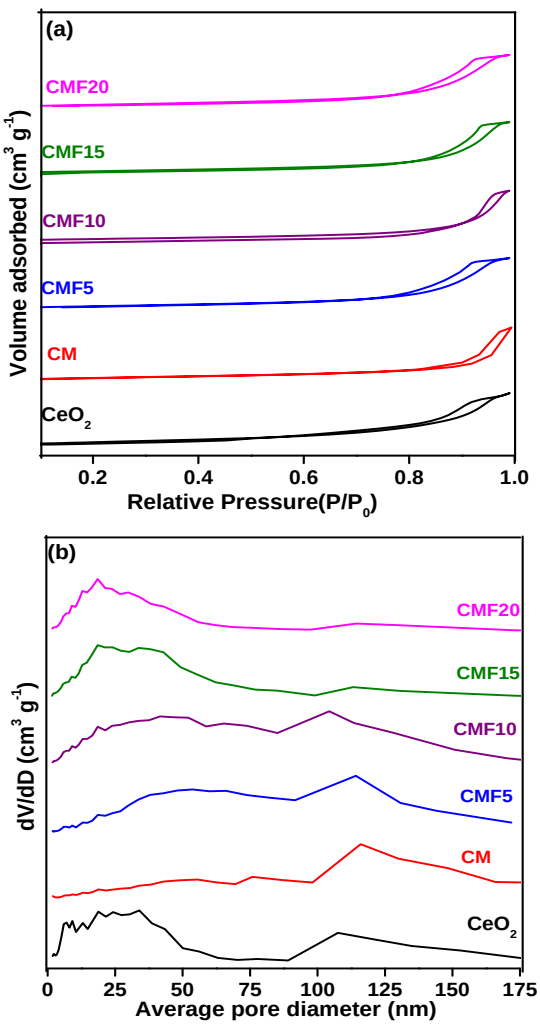

Fig. 2 (a) Nitrogen adsorption-desorption isotherms (b) pore size distributions of CeO_2, $Ce_{0.7}Mn_{0.3}O_{2-\delta}$ (CM), $Ce_{0.65}Mn_{0.3}Fe_{0.05}O_{2-\delta}$ (CMF5), $Ce_{0.6}Mn_{0.3}Fe_{0.1}O_{2-\delta}$ (CMF10), $Ce_{0.55}Mn_{0.3}Fe_{0.15}O_{2-\delta}$ (CMF15), and $Ce_{0.5}Mn_{0.3}Fe_{0.2}O_{2-\delta}$ (CMF20) catalysts.

Table 1 The surface areas (SA), pore volume (cm^3g^{-1}), pore diameter (nm), crystallite size (nm), and lattice parameter (Å) of CeO_2 $Ce_{0.7}Mn_{0.3}O_{2-\delta}$ (CM), $Ce_{0.65}Mn_{0.3}Fe_{0.05}O_{2-\delta}$ (CMF5), $Ce_{0.6}Mn_{0.3}Fe_{0.1}O_{2-\delta}$ (CMF10), $Ce_{0.55}Mn_{0.3}Fe_{0.15}O_{2-\delta}$ (CMF15), and $Ce_{0.5}Mn_{0.3}Fe_{0.2}O_{2-\delta}$ (CMF20) catalysts.

Sample	Surface area (m^2g^{-1})	Average Pore volume (cm^3g^{-1})	Average Pore diameter (nm)	Crystallite size (nm)	Lattice parameter (Å)
CeO_2	41	0.11	9.8	8.92	5.413
CM	58	0.44	6.23	7.19	5.350
CMF5	108.5	0.57	11.1	7.02	5.310
CMF10	107.5	0.54	21.9	5.89	5.270
CMF15	103.5	0.55	14.7	6.92	5.260
CMF20	125.6	0.51	13.5	6.55	5.220

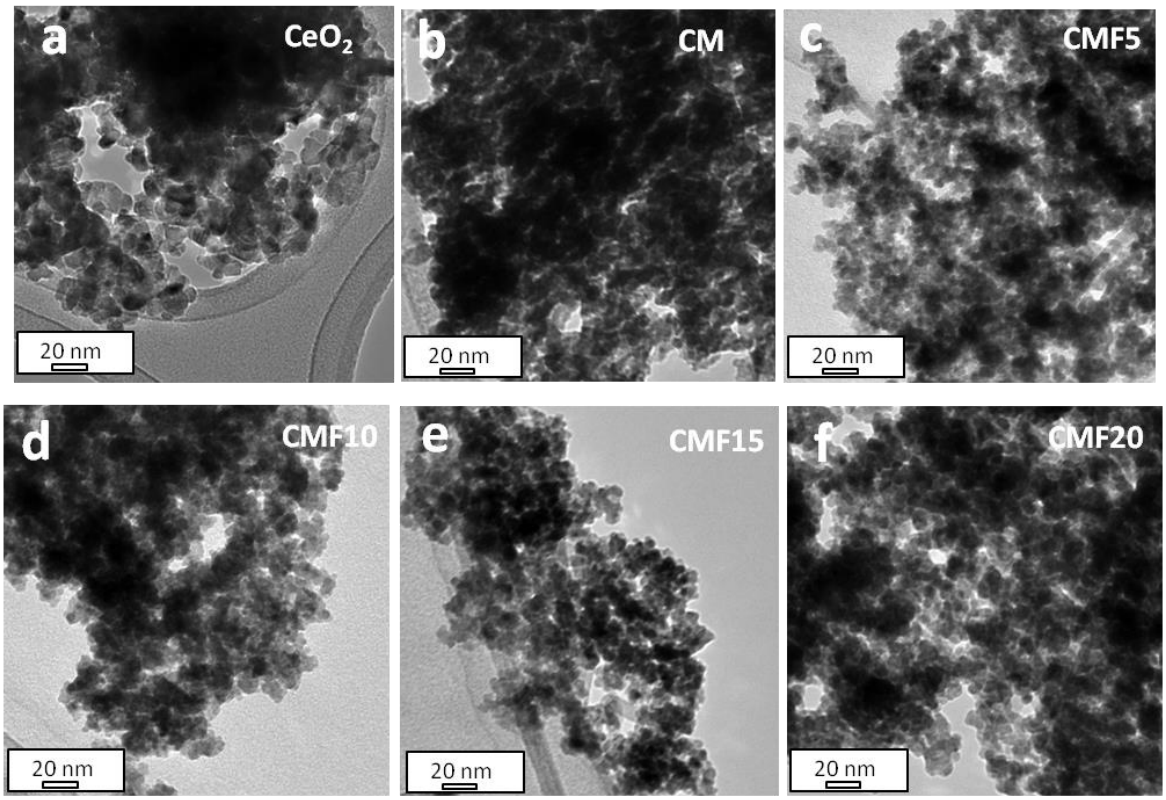

Fig. 3 TEM images of (a) CeO_2, (b) $Ce_{0.7}Mn_{0.3}O_{2-\delta}$ (CM), (c) $Ce_{0.65}Mn_{0.3}Fe_{0.05}O_{2-\delta}$ (CMF5), (d) $Ce_{0.6}Mn_{0.3}Fe_{0.1}O_{2-\delta}$ (CMF10), (e) $Ce_{0.55}Mn_{0.3}Fe_{0.15}O_{2-\delta}$ (CMF15), and (f) $Ce_{0.5}Mn_{0.3}Fe_{0.2}O_{2-\delta}$ (CMF20) catalysts.

of the unit cell parameter versus Fe (x=0, 0.05, 0.1, 0.15, or 0.20) content can be noticed (Table 1), which is in agreement with Vegard's law.[32] The observed phenomena can be explained through two possibilities. On one hand, it may be due to lattice constriction effect or synergetic interaction of Mn^{x+}, Fe^{3+}, and Ce^{4+} ions, which is resulting from the successful substitution of Ce^{4+} (0.97 Å) by Mn^{x+} (Mn^{2+} = 0.83Å, Mn^{3+} = 0.65Å, Mn^{4+} = 0.53Å) and Fe^{3+} (0.65 Å) ions, thereby the formation of $Ce_{0.7}Mn_{0.3}O_{2-\delta}$ and $Ce_{0.7-x}Mn_{0.3}Fe_xO_{2-\delta}$ solid solutions, respectively. On the other hand, when a Ce^{4+} ion is substituted by a Mn^{x+} or Fe^{3+}, a O vacancy will be formed to achieve electrical neutrality. Therefore an increase in the Fe content had enhanced the O vacancies which resulted in lattice contraction. Further, the intervalence charge transfer between Mn and/or Fe dopants could

cause significant alteration in the oxygen vacancy concentration. This would possibly enhance the catalytic properties. Additionally, the Ce, Mn, and Fe elemental compositions, which were present in the $Ce_{0.7-x}Mn_{0.3}Fe_xO_{2-\delta}$ solid solutions, were determined by ICP-OES analysis and the results are described in Table S1. It can be concluded that the calculated compositions are well matched with the designated chemical formulae.

The morphology of as-prepared pure CeO_2 and CM samples were determined using TEM as shown in Fig. 3a and Fig. 3b, respectively. It can be observed that the average particle size of CeO_2 is about ~12 nm, which is close to the values obtained from the Scherrer equation (Table 1). The particle size of CM sample is about ~8 nm, which is also a close match with the calculated average crystallite size from XRD. Fig 3c–f show the TEM images of the CMF samples having the compositions of $Ce_{0.65}Mn_{0.3}Fe_{0.05}O_{2-\delta}$, $Ce_{0.6}Mn_{0.3}Fe_{0.1}O_{2-\delta}$, $Ce_{0.55}Mn_{0.3}Fe_{0.15}O_{2-\delta}$, and $Ce_{0.5}Mn_{0.3}Fe_{0.2}O_{2-\delta}$ solid solutions, respectively. Interestingly, the TEM images of the CMF samples show that the particle sizes were about ~5–7 nm, which is well consistent with the XRD results. It was obvious that the particle sizes of the CMF samples were smaller than those of CM and CeO_2 samples and also the products have spherical shapes, which may be due to the fact that the codoping of Mn^{x+} and/or Fe^{3+} in CeO_2 lattice stabilizes nanocrystals of the solid solution.

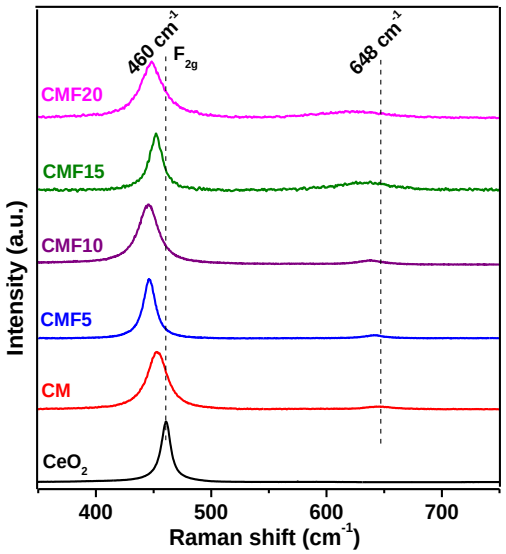

Fig. 4 Raman spectra of CeO_2, $Ce_{0.7}Mn_{0.3}O_{2-\delta}$ (CM), $Ce_{0.65}Mn_{0.3}Fe_{0.05}O_{2-\delta}$ (CMF5), $Ce_{0.6}Mn_{0.3}Fe_{0.1}O_{2-\delta}$ (CMF10), $Ce_{0.55}Mn_{0.3}Fe_{0.15}O_{2-\delta}$ (CMF15), and $Ce_{0.5}Mn_{0.3}Fe_{0.2}O_{2-\delta}$ (CMF20) catalysts.

The presence of Ce^{3+} or any dopants in the fluorite structure of CeO_2 generally generates oxygen vacancies in order to maintain electroneutrality. Raman spectroscopy is a useful technique to confer the information on the oxygen vacancies of oxide materials, especially ceria-containing solid solutions.[34] The Raman spectra of pure CeO_2, CM, and CMF samples are shown in Fig. 4. Usually, bulk CeO_2 has a strong Raman band (F_{2g}) at 460 cm^{-1}, which can be attributed to a symmetric breathing mode of the oxygen atoms surrounding each Ce^{4+} cation.[25] The Raman spectra of all CM and CMF samples display a strong band around this region, confirming the existence of fluorite structure of ceria in all the doped ceria samples. From Raman spectra, there are two typical characteristics in the main F_{2g} mode band, which differ from pure ceria. Firstly, the width of peak increased which is the result of either lattice defects or a consequence of electron molecular vibrational coupling arising from the increased concentration of defects in oxygen sub-lattice of CeO_2 and presence of magnetic ions in ceria lattice.[35–37] Second, the positions of CM and CMF samples differ relative to pure CeO_2. It can be obviously seen that the peak values shifted to the left side as Fe^{3+} doping concentration increased. This observed shift is powerful evidence of Mn and/or Fe incorporation in the lattice for the doped ceria samples, which could be attributed to the presence of oxygen vacancies. The extra oxygen vacancies could be generated due to the incorporation of $Mn^{4+/3+}$ and/or Fe^{3+} ions into the ceria fluorite lattice to compensate for the valence discrepancy between the M^{3+} (M= Mn, and/or Fe) and Ce^{4+} ions. Interestingly, the Fe_3O_4 peaks were observed to be absent for all the doped ceria samples. On the other hand, the peak observed at ~648 cm^{-1} attributed to the formation of Mn_3O_4.[25] However, the formation of isolated MnO_x and Fe_2O_3 crystallites are not detected by XRD, indicating some part of Mn-oxide phases might dispersed on the surface of the mixed oxide.[38, 39]

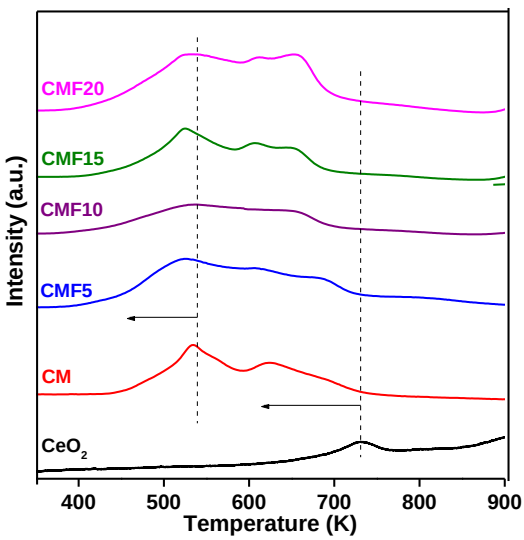

Fig. 5 H_2–TPR patterns of CeO_2, $Ce_{0.7}Mn_{0.3}O_{2-\delta}$ (CM), $Ce_{0.65}Mn_{0.3}Fe_{0.05}O_{2-\delta}$ (CMF5), $Ce_{0.6}Mn_{0.3}Fe_{0.1}O_{2-\delta}$ (CMF10), $Ce_{0.55}Mn_{0.3}Fe_{0.15}O_{2-\delta}$ (CMF15), and $Ce_{0.5}Mn_{0.3}Fe_{0.2}O_{2-\delta}$ (CMF20) catalysts.

In order to obtain information on the steps involved in the reduction processes, the redox properties of pure CeO_2, CM, and CMF samples were investigated by the H_2-TPR technique as

shown in Fig. 5. It is well known that the pure ceria has two reduction peaks, one at ~758 K, which can be ascribed to the surface reduction and later at 1005 K (not shown), which can be attributed to the complete reduction of Ce^{4+} into Ce^{3+}.[40] In case of CM sample, there are two reduction peaks, which appear at lower temperatures relative to pure CeO_2. According to literature, the low temperature peak observed at ~514 K could be attributed to the readily reducible and highly dispersed surface manganese species with the reduction of MnO_2/Mn_2O_3 to Mn_3O_4. The high temperature reduction peak observed at ~604 K can be assigned to the reduction of Mn_3O_4 to MnO and that of the surface ceria.[26] After introduction of Mn and/or Fe dopants together, the reduction peaks shifted to a low temperature region (<600 K) when compared to CM sample. This phenomenon can be due to the type of synergetic interaction between cerium oxide species and Mn and/or Fe oxides, which can create structural distortion and surface oxygen defects.[41] In addition, the peaks become broad and the reduction area under the peak increased as the Fe^{3+} doping concentration increases. According to H_2 consumption peak areas, the CMF samples could have more active oxygen species.[26] Therefore, a higher concentration of these surface active oxygen species can be expected to play a vital role when employing these catalysts for catalytic oxidation reactions.

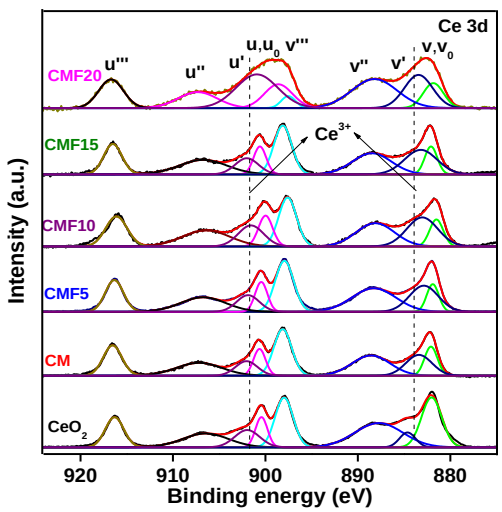

Fig. 6 Ce 3d XP spectra of CeO_2, $Ce_{0.7}Mn_{0.3}O_{2-\delta}$ (CM), $Ce_{0.65}Mn_{0.3}Fe_{0.05}O_{2-\delta}$ (CMF5), $Ce_{0.6}Mn_{0.3}Fe_{0.1}O_{2-\delta}$ (CMF10), $Ce_{0.55}Mn_{0.3}Fe_{0.15}O_{2-\delta}$ (CMF15), and $Ce_{0.5}Mn_{0.3}Fe_{0.2}O_{2-\delta}$ (CMF20) catalysts.

Further to verify the elementary oxidation states and surface compositions of each species within the synthesized samples, they were analysed using XPS. Fig. 6 shows the Ce 3d XPS profile of CeO_2, CM, and CMF samples. The XP spectra of Ce 3d could split into five spin-orbit doublets ($3d_{5/2}$ and $3d_{3/2}$) labelled as v_0, v, v′, v″, v‴, u_0, u, u′, u″, u‴. The signals v, v″, v‴, u, u″, u‴ can be assigned to Ce^{4+} species while those labelled v′ and u′ are related to Ce^{3+} species.[40, 42–44] It can be clearly observed that both Ce^{3+} and Ce^{4+} coexist in the catalysts, however, the primary valance is observed to be the 4+ oxidation state. It is worth noting that the intensity of Ce^{4+} peaks (v, v″, v‴, u, u″, u‴) of CMF samples is smaller than that of CM and pure CeO_2 samples, indicating that the concentration of $Ce^{3+}/(Ce^{3+} + Ce^{4+})$ on the surface of these samples is enhanced by the incorporation of Fe^{3+} and/or Mn^{x+} into the CeO_2 lattice.[45] In order to confirm this, the Ce^{3+} concentration was calculated by deconvolution of peaks and the obtained results are illustrated in Table S2. The CMF samples showed highest Ce^{3+} concentration compared to pure CeO_2 and CM samples, and the respective order is CMF20 > CMF15 > CMF10 > CMF5 > CM > CeO_2. It is well reported that the appearance of Ce^{3+} in the lattice could create lattice distortion, thereby generation of oxygen vacancies, and unsaturated chemical bonds on the catalyst surface.[46,47] These oxygen vacancies can be utilized for enhanced Hg^0 oxidation.

The O 1s XPS spectra of pure CeO_2, CM, and CMF samples are shown in Fig. 7. In case of pure CeO_2, the O 1s spectra can be fitted into two Gaussian peaks by deconvolution. The peak centered at ~529.4–530.2 eV is attributed to lattice oxygen (designated as O_I) while that located at ~531.4–532.1 eV can be attributed to surface-absorbed oxygen from the oxide defects or OH groups (designated as O_{II}).[25] In case of doped ceria samples, the additional peak located at ~533.5 eV (designated as O_{III}) can be attributed to chemisorbed water and/or carbonates on the catalyst surface.[48] As can be seen from Fig. 7, there is a shifting of the lattice oxygen peak towards lower binding energy values. It clearly indicates that the chemical environment of lattice oxygen was significantly changed after the Mn and/or Fe incorporation.[33] The lower binding energy of lattice oxygen could make the surface oxygen more labile, which could be beneficial for the low-temperature Hg^0 oxidation.

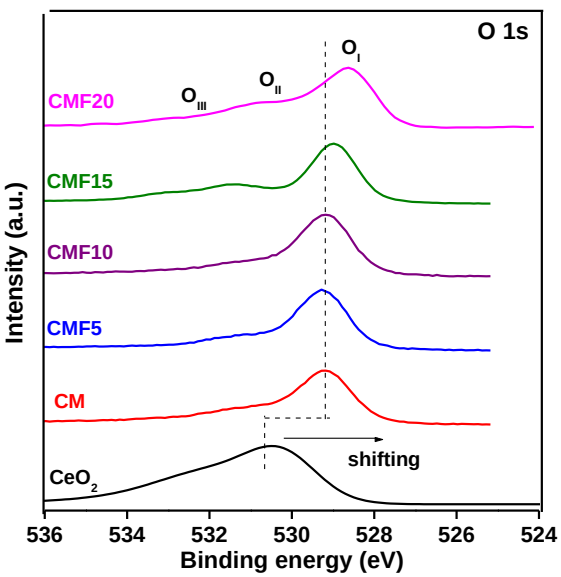

Fig. 7 O 1s XP spectra of CeO_2, $Ce_{0.7}Mn_{0.3}O_{2-\delta}$ (CM), $Ce_{0.65}Mn_{0.3}Fe_{0.05}O_{2-\delta}$ (CMF5), $Ce_{0.6}Mn_{0.3}Fe_{0.1}O_{2-\delta}$ (CMF10), $Ce_{0.55}Mn_{0.3}Fe_{0.15}O_{2-\delta}$ (CMF15), and, $Ce_{0.5}Mn_{0.3}Fe_{0.2}O_{2-\delta}$ (CMF20) catalysts.

The Mn 2p core level spectra of CM and CMF samples are shown in Fig. S2a, while the Fe 2p core level spectra for CMF samples are shown in Fig. S2b. The XPS profile of Mn 2p exhibited two peaks at ~653.2 and ~642.2 eV, which can be attributed to Mn $2p_{1/2}$ and Mn $2p_{3/2}$ states, respectively. The broad Mn $2p_{3/2}$ can be divided into three characteristic peaks, which can be assigned to Mn^{2+} (640.4 eV), Mn^{3+} (642.2 eV), and Mn^{4+} (643.5 eV), respectively, which is matched with literature.[49] This implies the co-existence of Mn^{2+}, Mn^{3+}, and Mn^{4+} ions at the surface of the catalysts. The presence of high valance having manganese species could be enhanced mercury removal efficiency. The binding energy of Fe $2p_{3/2}$ and Fe $2p_{1/2}$ core level spectra of CMF samples is observed at ~710.8 and ~724.2 eV (Fig. S2b). They can be attributed to the +3 oxidation states of Fe. In addition, the peak separation between $2p_{3/2}$ and $2p_{1/2}$ is approximately 14 eV, which confirms that Fe is in the oxide phase rather than in metallic form.[50,51]

3.2 Hg^0 oxidation and adsorption performances

3.2.1 Effect of Fe loading content under different flue gas conditions

In order to investigate the efficiency of Hg^0 oxidation (E_{oxi}) and adsorption (E_{ads}) over the investigated catalysts, some blank tests (where no catalyst was present) were performed to determine the extent of Hg^0 oxidation under HCl and O_2 atmosphere at 423 K (Fig. S3). The result showed that the amount of oxidized mercury was around 16 % , which can be due to the presence of oxidant species such as HCl and O_2 in the flue gas. Fig. S4 shows that the total amount of mercury (Hg_T) was approximately the same as the amount of inlet Hg^0, since homogeneous reactions in the given reaction condition are hindered by a very high energy barrier.[52] Fig. 8a, 8b, 8c represents the effect of Fe doping on Hg^0 removal efficiencies (E_{oxi} and E_{ads}) in presence of HCl, O_2, and HCl/O_2 mix conditions, respectively. As shown in Fig. 8a, the E_{oxi} in HCl conditions was approximately in the range of 43–86.5 % for the CMF samples, whereas the CM and CeO_2 samples showed 11.2 and 14.6 %, respectively. Among all the CMF samples, the CMF20 sample showed E_{oxi} of 86.5 %, which was superior to that of CM and pure CeO_2 samples. It was clear that the codoping of Mn and Fe significantly enhanced the Hg^0 removal performance of CeO_2. Furthermore, it can be observed that as the Fe content increases to 20%, the oxidation efficiency also increased to 86.5 %. The results clearly demonstrate that a higher loading content produces more Ce^{3+} concentration, thereby more surface oxygen vacancies in the ceria lattice, which is supported by XPS results. As a result CMF20 catalyst produced relatively more active sites for catalytic reactions and thus enhances the Hg^0 oxidation efficiency. Furthermore, it is clearly observed that although the E_{oxi} increases with increasing Fe content, the rate at which E_{oxi} increases with respect to Fe content was observed to decrease significantly when the Fe content increased from 15% to 20%, as shown in Fig. S5. On the other hand, when the catalysts were tested for their Hg^0 removal performance in the presence of O_2 atmosphere, it was found that E_{oxi} of CM and CMF samples were less than 15%, while their E_{ads} were more than 90 %. This is postulated to be due to the high active oxygen content present in the CMF samples. Fig. 8c shows the catalyst performance when tested under HCl/O_2 mixture. It is observed that Hg^0 oxidation as

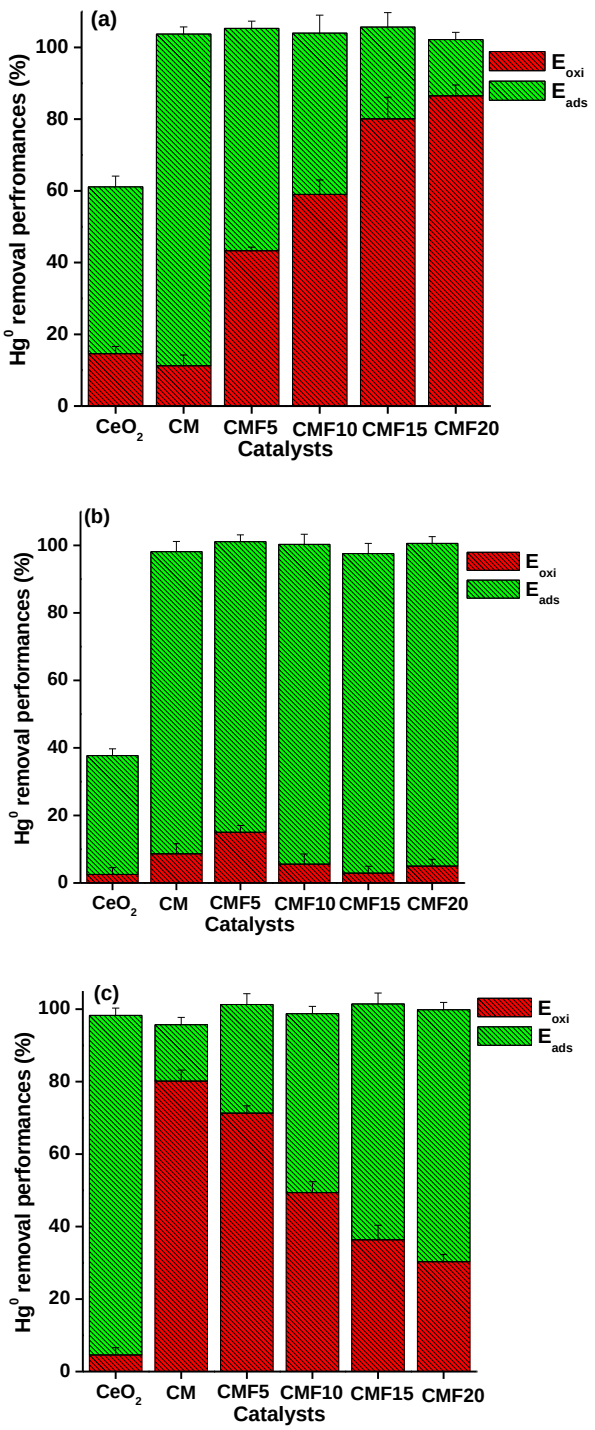

Fig. 8 Hg^0 removal performances over CeO_2, $Ce_{0.7}Mn_{0.3}O_{2-\delta}$ (CM), $Ce_{0.65}Mn_{0.3}Fe_{0.05}O_{2-\delta}$ (CMF5), $Ce_{0.6}Mn_{0.3}Fe_{0.1}O_{2-\delta}$ (CMF10), $Ce_{0.55}Mn_{0.3}Fe_{0.15}O_{2-\delta}$ (CMF15), and $Ce_{0.5}Mn_{0.3}Fe_{0.2}O_{2-\delta}$ (CMF20) catalysts under different flue gas conditions (a) HCl (b) O_2 (c) HCl and O_2.

well as adsorption occurred. Generally, Hg^0 cannot be directly oxidized by HCl in the absence of O_2.[53], therefore the available surface oxygen (observed in our XPS data) species leads to formation of active chlorine species, which can be responsible for Hg^0 oxidation. This observation further explains the data presented in Fig. 8a, where the CMF catalysts showed better Hg^0 oxidation performances in presence of HCl. The data indicates that when O_2 is introduced into the catalyst bed individually or together with HCl vapor, the weakly adsorbed Hg^0 reacts with surface oxygen to form mercuric oxide (HgO) instead of the preferred water soluble form of oxidize mercury (i.e. $HgCl_2$).[54] However, some portion of Hg^0 can be converted to $HgCl_2$ in presence of HCl and O_2, however but it might not exist on the surface of the catalyst because of its easy sublimation at the operating temperature of 423 K.[55–57] The plausible mechanism involved in this process is clearly represented as a scheme and shown in Fig. 9. Overall, the Hg^0 removal performances (adsorption and oxidation) of the CMF samples were prominent in all conditions. Moreover, the addition of Fe dopant is found to have produced well dispersed active sites and more surface oxygen, which all contribute toward superior Hg^0 removal performance of the developed catalysts, in particular CMF20 catalyst.

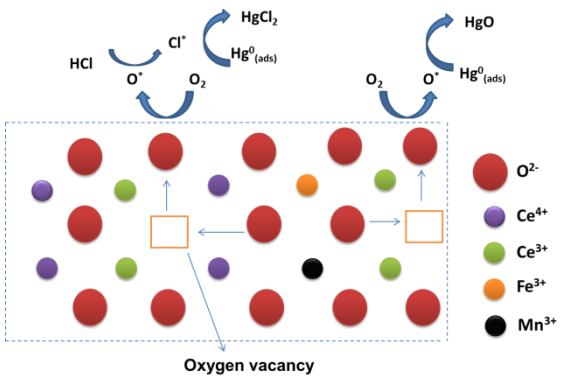

Fig. 9 Plausible mechanism for Hg^0 removal on CMF catalyst.

3.3 Effect of individual flue gas components

3.3.1 Effect of HCl

Generally, the high levels of mercury oxidation are most strongly correlated with high chlorine concentrations in the coal-fired power plant flue gas.[2,58] Therefore, the effect of HCl concentration on Hg^0 conversion of CMF20 catalyst developed in this study is investigated and the results are shown in Fig. 10. With the increase of HCl concentration from 5 ppm to 20 ppm, the E_{oxi} increased from 60 to 95 %. On the other hand, the E_{ads} is observed to decrease from 42 to 7 % for the same change in HCl concentration. It clearly indicates that formation of surface defects or oxygen vacancies reinforced the formation of active chlorine species, which are responsible for Hg^0 oxidation in the presence of HCl.[1,13] Additionally, the E_{oxi} is observed to increase only slightly when the HCl concentration is increased from 10 to 20 ppm. It can be due to the constant amount of active sites for both Hg^0 and HCl species on the surface of the samples. Overall, the Hg^0 oxidation mechanism of the developed CMF20 catalyst is likely to follows the Langmuir–Hinshelwood mechanism, in which the activated oxygen and chlorine species on catalyst surface react with adsorbed Hg^0 to form Hg^{2+} [18,59] as follows.

$$2HCl + O^* \rightarrow 2Cl^* + H_2O \quad (3)$$

$$Hg^0_{(g)} \rightarrow Hg^0_{(ads)} \quad (4)$$

$$Hg^0_{(ads)} + Cl^* \rightarrow HgCl^* \quad (5)$$

$$HgCl^* + Cl^* \rightarrow HgCl_2 \quad (6)$$

$$Cl^* + Cl^* \rightarrow Cl_2 \quad (7)$$

$$Hg^0_{(g)} + Cl_2 \rightarrow HgCl + Cl^* \quad (8)$$

$$HgCl + Cl_2 \rightarrow HgCl_2 + Cl^* \quad (9)$$

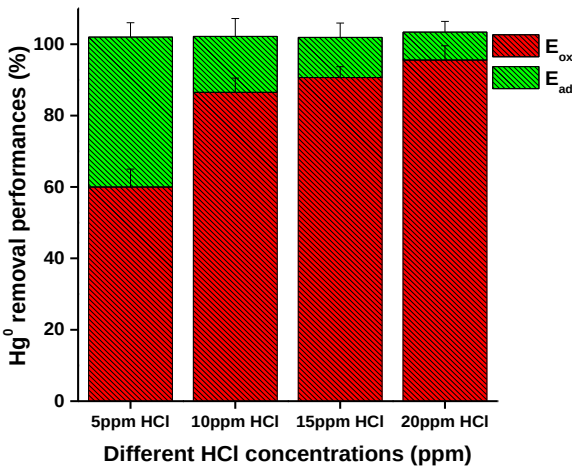

Fig. 10 Effect of HCl on Hg^0 removal performances over $Ce_{0.5}Mn_{0.3}Fe_{0.2}O_{2-\delta}$ (CMF20) catalyst.

3.3.2 Effect of O_2

The E_{oxi} and E_{ads} changing with O_2 concentration was studied over CMF20 catalyst at an operating temperature of 473 K as shown in Fig. 11. It can be clearly observed that the O_2 concentration affects the extent of E_{oxi} and E_{ads} of the developed CMF20 catalyst during Hg^0 oxidation reactions. Li et. al has previously reported that adsorbed Hg on the Mn–Ce/Ti catalyst can be explained by the Mars–Maessen mechanism.[18] It clearly explains that Hg^0 reacts with lattice oxygen on the catalyst surface to form weakly bonded speciation Hg–O–MnO_{x-1} or reacts with surface oxygen to form HgO.[1] However in the presence of HCl, the scenario is different. The active Cl* may generate due to the presence of lattice oxygen from the catalyst. Initially, the CMF20 catalyst was tested towards 10 ppm HCl and 3% O_2 conditions at 473 K and found that the E_{oxi} and E_{ads} were 4.53 and 95.3 %, respectively. Due to the high E_{ads}, it can be concluded that Hg^0 was converted to Hg^{2+} in the form of HgO. Unlike $HgCl_2$ which sublimes easily, HgO has a low vapor pressure which inhibits it from reaching the KCl tarps designed

for oxidized mercury and thus it can be adsorbed on the catalyst. This is further evidenced by the fact that as the concentration of O_2 decreases from 3% to 0.75 %, the E_{ads} decreased and E_{oxi} increased. The observed E_{oxi} and E_{ads} in the presence of 10 ppm HCl and 0.75% O_2 gas mixture were 68 and 31%, respectively. It was clear that the oxidised from of mercury can exist in two forms such as HgO or $HgCl_2$ and this form is completely depends on the concentrations of flue gases.

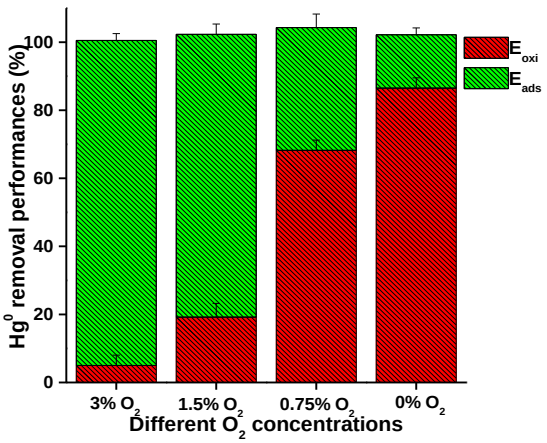

Fig. 11 Effect of O_2 on Hg^0 removal performances over $Ce_{0.5}Mn_{0.3}Fe_{0.2}O_{2-\delta}$ (CMF20) catalyst.

The adsorption of elemental mercury by metal oxides can be explained by Mars–Maessen mechanism.[60] In this mechanism, adsorbed Hg^0 would react with a lattice oxidant (either active O* or Cl*) that is replenished from the gas phase. The reactions, which happened during elemental mercury adsorption by the CMF20 catalyst, were described as follows

$$Hg^0_{(g)} \leftrightarrow Hg^0_{(ads)} \quad (10)$$

$$Hg^0_{(ads)} + Ce(IV)–O_x \rightarrow HgO_{(ads)} + Ce(III)–O_{x-1} \quad (11)$$

$$Ce(III)–O_{x-1} + 1/2\ O_2 \rightarrow Ce(IV)–O_x \quad (12)$$

$$Hg^0_{(ads)} + Mn^{4+} + O^* \rightarrow HgO_{(ads)} + Mn^{3+} \quad (13)$$

$$Hg^0_{(ads)} + Fe^{3+} + O^* \rightarrow HgO_{(ads)} + Fe^{2+} \quad (14)$$

$$Mn^{3+} + 1/2O_2 \rightarrow Mn^{4+} + O^* \quad (15)$$

$$Fe^{2+} + 1/2O_2 \rightarrow Fe^{3+} + O^* \quad (16)$$

According to reaction 10, the Hg^0 first adsorbs on the active sites of the catalyst surface. The adsorbed mercury is then oxidized to HgO by reaction (11). Reaction (12) then follows where the Ce(IV)–O_x component of the catalyst is regenerated. In addition, the adsorbed Hg^0 could also react with lattice or surface oxygen that is provided by the dispersed Mn and/or Fe oxides on the CMF20 catalyst. The proceeding reactions (13–16) demonstrate the Hg^0 oxidation and regeneration of the Mn and Fe components of the catalyst that is thought to occur in presence of O_2 atmosphere. During reoxidization, some cation vacancies may also be recovered.[61] Therefore, it can be concluded that the incorporation of Mn and Fe together in the CeO_2 lattice is advantageous for achieving better Hg^0 removal efficiencies.

3.3.3 Effect of NH_3

In order to understand the plausible mechanisms involved in the inhibition of Hg^0 removal by NH_3 over CMF20 catalyst, 300 ppm NH_3 was added into the system. The effect of NH_3 was tested in two different conditions such as NH_3+HCl and NH_3+O_2 and the resulting E_{oxi} and E_{ads} of the CMF20 catalyst is presented in Fig. 12. It can be observed that the addition of 300 ppm NH_3 and 3% O_2 gas mixture resulted in a significant decrease of E_{ads} from 95 to 60 %. On the other hand, the NH_3 and HCl gas mixture also showed obvious inhibition on E_{oxi} and E_{ads}. The E_{oxi} was found to reduce from 86 to 35% for CMF20 catalyst. It is well reported in the literature that NH_3 is the dominant adsorbed specie, when it exists with other acidic components such as HCl and O_2 in flue gas.[8] Therefore, it can be concluded that NH_3 can strongly compete for active sites to adsorb on the catalyst surface, thereby inhibits Hg^0 oxidation and adsorption.[62,63] Further, due to its basic nature, NH_3 can react with the oxidised mercury (HgO and/or $HgCl_2$), thereby forming elemental form (Hg^0), which is the major issue when SCR catalysts employed in the industrial power plants.[10]

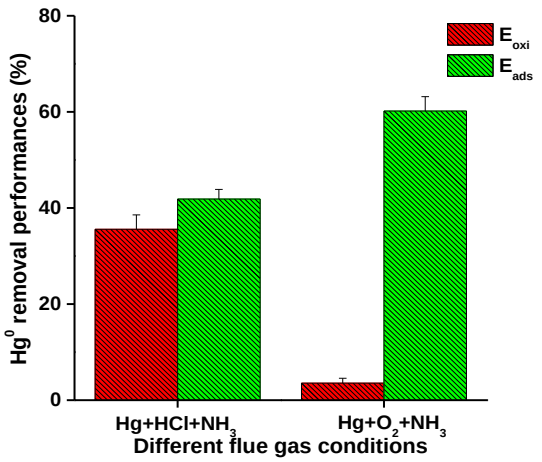

Fig. 12 Effect of NH_3 on Hg^0 removal performances over $Ce_{0.5}Mn_{0.3}Fe_{0.2}O_{2-\delta}$ (CMF20) catalyst.

4. Conclusions

In this study, we successfully prepared Mn and Fe codoped CeO_2 solid solutions by a simple and facile coprecipitation method. The developed $Ce_{0.7-x}Mn_{0.3}Fe_xO_{2-\delta}$ catalysts were highly active toward Hg^0 oxidation and adsorption at low flue gas temperatures when compared to pure CeO_2 and CM samples. Among the developed catalysts, the CMF20 catalyst (synthesised with 20% Fe content in the solution) exhibited more than 85% Hg^0 oxidation efficiency at 423 K. From the XRD and XPS

studies, the high conversion efficiency was attributed to the relatively higher surface oxygen concentration, oxygen vacancies as well as the strong interaction between Mn and/or Fe dopants and CeO_2. From H_2–TPR studies, it was deduced that the presence of Fe ion in $Ce_{0.7-x}Mn_{0.3}Fe_xO_{2-\delta}$ solid solution brought down the temperature of H_2-uptake. As a result, the Mn and Fe co-doped CeO_2 samples showed enhanced redox behaviour compared to CM and pure CeO_2 samples. In our future work, the effect of the components in the flue gas such as NO_x, SO_2, SO_3, and H_2O vapor on elemental mercury oxidation and adsorption by CMF samples will be investigated.

Acknowledgement

D. J. thanks RMIT University for providing the RMIT-IICT postgraduate Scholarship and RMIT microscopy and microanalysis facility (RMMF) for allowing the use of their comprehensive facilities and services.

†Electronic supplementary information (ESI) available: Detailed information about the chemical compositions and surface atomic concentrations, experimental diagram, Mn 2p and Fe 2p XPS profiles of Mn doped CeO_2 and Mn and/or Fe codoped CeO_2 solid solutions, Hg^0 oxidation experiment without catalyst, calibration experiments for Hg^0_{inlet}, and relation between Fe doping versus E_{oxi} increase rate.

References

1 H. Li, C.-Y. Wu, Y. Li, L. Li, Y. Zhao, J. Zhang, *J. Hazard. Mater.*, 2012, **243**, 117–123.
2 Y. Zheng, A.D. Jensen, C. Windelin, F. Jensen, *Prog. Energy Combust. Sci.*, 2012, **38**, 599–629.
3 Y.M. Sabri, S.J. Ippolito, A.J. Atanacio, V. Bansal, S.K. Bhargava, *J. Mater. Chem.*, 2012, **22**, 21395–21404.
4 X.-y. Hua, J.-s. Zhou, Q. Li, Z.-y. Luo, K.-f. Cen, Energy Fuels, 2010, **24**, 5426–5431.
5 E.J. Granite, C.R. Myers, W.P. King, D.C. Stanko, H.W. Pennline, *Ind. Eng. Chem. Res.*, 2006, **45**, 4844–4848.
6 S. Tao, C. Li, X. Fan, G. Zeng, P. Lu, X. Zhang, Q. Wen, W. Zhao, D. Luo, C. Fan, *Chem. Eng. J.*, 2012, **210**, 547–556.
7 A.P. Jones, J.W. Hoffmann, D.N. Smith, T.J. Feeley, J.T. Murphy, *Environ. Sci. Technol.*, 2007, **41**, 1365–1371.
8 A.A. Presto, E.J. Granite, *Environ. Sci. Technol.*, 2006, **40** 5601–5609.
9 V.R. Choudhary, D.K. Dumbre, S.K. Bhargava, *Ind. Eng. Chem. Res.*, 2009, **48**, 9471–9478
10 B.-A. Dranga, L. Lazar, H. Koeser, *Catalysts*, 2012, **2**, 139–170.
11 J. Yang, Q. Yang, J. Sun, Q. Liu, D. Zhao, W. Gao, L. Liu, *Catal. Commun.*, 2015, **59**, 78–82.
12 A. Suarez Negreira, J. Wilcox, *J. Phys. Chem. C*, 2012, **117**, 1761–1772.
13 H. Li, C.-Y. Wu, Y. Li, J. Zhang, *Environ. Sci. Technol.*, 2011, **45**, 7394–7400.
14 F. Kong, J. Qiu, H. Liu, R. Zhao, Z. Ai, *J. Environ. Sci.*, 2011, **23**, 699–704.
15 Z. Wu, R. Jin, Y. Liu, H. Wang, *Catal. Commun.*, 2008, **9**, 2217–2220.
16 R. Jin, Y. Liu, Z. Wu, H. Wang, T. Gu, *Chemosphere*, 2010, **78**, 1160–1166.
17 S.M. Lee, K.H. Park, S.C. Hong, *Chem. Eng. J.*, 2012, **195–196**, 323–331.
18 H. Li, C.-Y. Wu, Y. Li, J. Zhang, *Appl. Catal., B*, 2012, **111–112**, 381–388.
19 D. Jampaiah, K.M. Tur, S.J. Ippolito, Y.M. Sabri, J. Tardio, S.K. Bhargava, B.M. Reddy, *RSC Adv.*, 2013, **3**, 12963–12974.
20 V.M. Shinde, G. Madras, *Appl. Catal. B*, 2013, **138–139**, 51–61.
21 X. Liu, L. Han, W. Liu, Y. Yang, *Eur. J. Inorg. Chem.*, 2014, **31**, 5370–5377.
22 A.B. Kehoe, D.O. Scanlon, G.W. Watson, *Chem. Mater.*, 2011, **23**, 4464–4468.
23 B.V. Reddy, F. Rasouli, M.R. Hajaligol, S.N. Khanna, *Fuel*, 2004, **83**, 1537-1541.
24 J. Q. Sun, K. S. Uhrich and R. L. Schulz, *Prepr. Pap.-Am. Chem. Soc., Div. Fuel Chem.*, 2003, **48**, 774–776.
25 P. Venkataswamy, K.N. Rao, D. Jampaiah, B.M. Reddy, *Appl. Catal., B*, 2015, **162**, 122–132.
26 P. Venkataswamy, D. Jampaiah, K.N. Rao, B.M. Reddy, *Appl. Catal., A*, 2014, **488**, 1– 10.
27 Y.-W. Ju, S. Ida, T. Ishihara, *RSC Adv.*, 2013, **3**, 10508–10515.
28 S. Cai, D. Zhang, L. Zhang, L. Huang, H. Li, R. Gao, L. Shi, J. Zhang, Catal. Sci. Technol. 4 (2014) 93–101.
29 I. Moog, C. Feral-Martin, M. Duttine, A. Wattiaux, C. Prestipino, S. Figueroa, J. Majimel, A. Demourgues, *J. Mater. Chem., A*, 2014, **2**, 20402–20414.
30 G. Xiao, S. Li, H. Li, L. Chen, *Microporous and Mesoporous Mater.*, 2009, **120**, 426–431.
31 G.-R. Li, D.-L. Qu, L. Arurault, Y.-X. Tong, *J. Phys. Chem. C*, 2009, **113**, 1235–1241.
32 R.S. Kalubarme, H.S. Jadhav, C.-N. Park, K.-N. Jung, K.-H. Shin, C.-J. Park, J. Mater. Chem., A. 2 (2014) 13024–13032.
33 P. Sudarsanam, B. Mallesham, D.N. Durgasri, B.M. Reddy, *RSC Adv.*, 2014, **4**, 11322–11330.
34 B.M. Reddy, L. Katta, G. Thrimurthulu, *Chem. Mater.*, 2009, **22**, 467–475.
35 S. Phokha, S. Pinitsoontorn, S. Maensiri, *Nano-Micro Lett.*, 2013, **5**, 223–233.
36 Z.D. Dohčević-Mitrović, M.J. Šćepanović, M.U. Grujić-Brojčin, Z.V. Popović, S.B. Bošković, B.M. Matović, M.V. Zinkevich, F. Aldinger, *Solid State Commun.*, 2006, **137**, 387–390.
37 Z.D. Dohčević-Mitrović, N. Paunović, M. Radović, Z.V. Popović, B. Matović, B. Cekić, V. Ivanovski, *Appl. Phys. Lett.*, 2010, **96**, 203104–203106.
38 M. Kang, J. Zhang, C. Wang, F. Wang, N. Zhao, F. Xiao, W. Wei, Y. Sun, RSC Adv. 2013, **3**, 18878–18885.
39 P. Sudarsanam, P.R. Selvakannan, S.K. Soni, S.K. Bhargava, B.M. Reddy, *RSC Adv.*, 2014, **4**, 43460–43469.
40 X. Yao, C. Tang, Z. Ji, Y. Dai, Y. Cao, F. Gao, L. Dong, Y. Chen, *Catal. Sci. Technol.*, 2013, **3**, 688–698.
41 Y. Sheng, Y. Zhou, H. Lu, Z. Zhang, Y. Chen, Chinese *J. Catal.*, 2013, **34**, 567–577.
42 N. Paunovic, Z. Dohcevic-Mitrovic, R. Scurtu, S. Askrabic, M. Prekajski, B. Matovic, Z.V. Popovic, *Nanoscale*, 2012, **4**, 5469–5476.

43 Q. Dai, S. Bai, Z. Wang, X. Wang, G. Lu, *Appl. Catal., B*, 2012, **126**, 64–75.

44 D. Devaiah, D. Jampaiah, P. Saikia, B.M. Reddy, *J. Ind. Eng.Chem.*, 2014, **20**, 444–453.

45 E. Ginting, S. Hu, J.E. Thorne, Y. Zhou, J. Zhu, J. Zhou, *Appl. Surf. Sci.*, 2013, **283**, 1–5.

46 P. Wang, S. Su, J. Xiang, H. You, F. Cao, L. Sun, S. Hu, Y. Zhang, *Chemosphere*, 2014, **101**, 49–54.

47 Q. Wan, L. Duan, K. He, J. Li, *Chem. Eng. J.*, 2011, **170**, 512–517.

48 X. Yao, Q. Yu, Z. Ji, Y. Lv, Y. Cao, C. Tang, F. Gao, L. Dong, Y. Chen, *Appl. Catal., B*, 2013, **130–131**, 293–304.

49 Z. Wang, G. Shen, J. Li, H. Liu, Q. Wang, Y. Chen, *Appl. Catal., B*, 2013, **138–139**, 253–259.

50 Z. Zhang, D. Han, S. Wei, Y. Zhang, *J. Catal.*, 2010, **276**, 16–23.

51 T. Yamashita, P. Hayes, *Appl. Surf. Sci*., 2008, **254**, 2441–2449.

52 H. Li, Y. Li, C.-Y. Wu, J. Zhang, *Chem. Eng. J.*, 2011, **169**, 186–193.

53 W. Gao, Q. Liu, C.-Y. Wu, H. Li, Y. Li, J. Yang, G. Wu, *Chem. Eng. J.*, 2013, **220**, 53–60.

54 Y. Li, P.D. Murphy, C.-Y. Wu, K.W. Powers, J.-C.J. Bonzongo, *Environ. Sci. Technol.*, 2008, **42**, 5304–5309.

55 D. Liu, *Carbon* 1993, **31**, 1237–1242.

56 P. Wang, S. Hu, J. Xiang, S. Su, L. Sun, F. Cao, X. Xiao, A. Zhang, *P. Combust. Inst.* 2015, **35**, 2847–2853.

57 M. A. Lopez-Anton, Y. Yuan, R. Perry, M. M. Maroto-Valer, *Fuel*, 2010, **89**, 629–634.

58 K.C. Galbreath, C.J. Zygarlicke, *Fuel Process. Technol.*, 2000, **65–66**, 289–310.

59 K.B. Ko, Y. Byun, M. Cho, W. Namkung, D.N. Shin, D.J. Koh, K.T. Kim, *Chemosphere*, 2008, **71**, 1674–1682.

60 E.J. Granite, H.W. Pennline, R.A. Hargis, *Ind. Eng. Chem. Res*,. 2000, **39**, 1020–1029.

61 L. Xing, Y. Xu, Q. Zhong, Energy Fuels, 2012, **26**, 4903–4909.

62 H. Kamata, S.-i. Ueno, T. Naito, A. Yukimura, *Ind. Eng. Chem. Res.*, 2008, **47**, 8136–8141.

63 H. Kamata, S.-i. Ueno, N. Sato, T. Naito, Fuel Process. Technol., 2009, **90**, 947–951.